Nanoscale

Accepted Manuscript

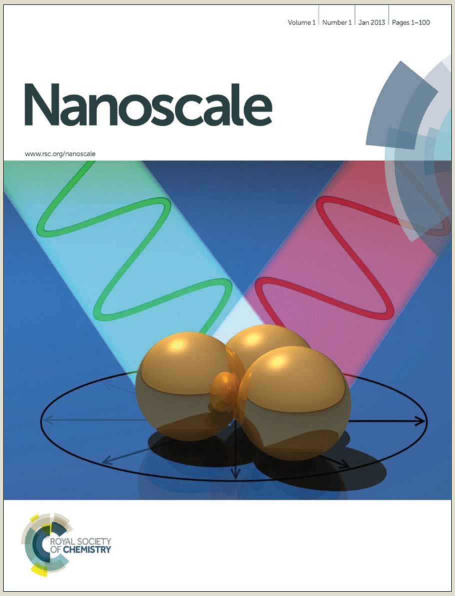

ROYAL SOCIETY OF CHEMISTRY

www.rsc.org/nanoscale

Nanoscale RSCPublishing

ARTICLE

Oxygen orders differently under graphene: new superstructures on Ir(111)

Cite this: DOI: 10.1039/x0xx00000x

A. J. Martínez-Galera [a], U. A. Schröder [a], F. Huttmann [a], W. Jolie [a], F. Craes [a], C. Busse [a], V. Caciuc [b], N. Atodiresei [b], S. Blügel [b] and T. Michely[a]

Received 00th January 2012,
Accepted 00th January 2012

DOI: 10.1039/x0xx00000x

www.rsc.org/

Using scanning tunneling microscopy, the oxygen adsorbate superstructures on bare Ir(111) are identified and compared to the ones formed by intercalation in between graphene and the Ir(111) substrate. For bare Ir(111) we observe O-(2×2) and O-(2×1) structures, thereby clarifying a persistent uncertainty about the existence of these structures and the role of defects for their stability. For the case of graphene-covered Ir(111), oxygen intercalation superstructures can be imaged through the graphene monolayer by choosing proper tunneling conditions. Depending on the pressure, temperature and duration of O_2 exposure as well as on the graphene morphology, O-(2×2), O-($\sqrt{3}\times\sqrt{3}$)-R30º, O-(2×1) and O-($2\sqrt{3}\times2\sqrt{3}$)–R30º superstructures with respect to Ir(111) are observed under the graphene cover. Two of these structures, the O-($\sqrt{3}\times\sqrt{3}$)-R30º and the ($2\sqrt{3}\times2\sqrt{3}$)–R30º structure are only observed when the graphene layer is on top. Phase coexistence and formation conditions of the intercalation structures between graphene and Ir(111) are analyzed. The experimental results are compared to density functional theory calculations including dispersive forces. The existence of these phases under graphene and their absence on bare Ir(111) are discussed in terms of possible changes in the adsorbate-substrate interaction due to the presence of the graphene cover.

Introduction

Simultaneously with the rise of graphene (Gr) to a prime area in solid state research, the growth of Gr on transition metals has become a topic of substantial interest [1, 2]. Among the possible substrates for Gr epitaxy, Ir(111) is exceptional, as it enables growth of Gr only weakly coupled to the substrate with perfect alignment to it over macroscopic dimensions [3-5]. These properties make Gr/Ir(111) a popular system for controlled surface science studies using averaging or local methods. Modifying the properties of Gr/Ir(111) by intercalation of atoms or molecules has been proven to be a straightforward and versatile concept [6-15]. For three reasons oxygen is of specific interest as intercalant. First, oxygen has the potential to strongly interact with Gr under a variety of conditions leading to processes like combustion [16] or graphene oxide formation [17]. Second, oxygen is one of the few species inducing strong p-doping to Gr without hybridizing with Gr [7, 18]. Third, oxygen intercalation, with oxygen strongly bound to the substrate, effectively decouples Gr from its substrate, making its properties very close to those of freestanding Gr [6, 7]. The potential of this decoupling has been demonstrated, when for the first time standing wave patterns of Dirac electrons in Gr quantum dots could be observed unambiguously [18]. These properties motivated us to take a closer look to the real space structure of intercalated oxygen layers on Gr/Ir(111).

The chemisorption of oxygen to bare Ir(111) appears to be a well-studied case in surface science, at least when considering that the investigation of this system started in 1971 by Grant [19] and has led to numerous publications. Low energy electron diffraction (LEED) of the ordered ad-layer displays a diffraction pattern with a (2×2) periodicity [20-22]. Based on LEED I/V measurements, Chan and Weinberg [21] derived a threefold coordinated adsorption site on Ir(111), consistent with subsequent density functional theory (DFT) calculations that invariably find the fcc hollow as the preferred adsorption site [23-26]. Already early work interpreted the (2×2) LEED pattern to be the result of the superposition of three O-(2×1) superstructure domains consistent with a room temperature saturation coverage of 0.5 ML with respect to the Ir surface atom density [27-30]. Recently, this consensus was questioned theoretically: Zhang *et al.* [25] predict that the only three thermodynamically stable phases in the oxygen-Ir(111) system are the bare Ir(111) surface, the O-(2×2) structure with 0.25 ML coverage as well as the bulk oxide. Bianchi *et al.* [31] find a room temperature saturation coverage of 0.38±0.04 ML through a high resolution x-ray photoelectron spectroscopy (XPS) study. The authors conclude that the (2×1) structure cannot be obtained without a certain degree of disorder and that a long range ordered structure with 0.5 ML coverage is at room temperature unstable due to intrinsic properties of the O-Ir interface. Grånäs *et al.* [6] estimated with XPS a saturation coverage of 0.45±0.02 ML, much closer to what is expected for a perfect (2×1) structure, and with Ir 4f core level components consistent with an O-(2×1) structure. It is therefore timely to clarify the stability of the O-(2×2) and O-(2×1) superstructures and the role of defects in these structures through a real space approach. We will show here that the O-(2×1) structure is indeed a stable structure at or close to saturation and may be formed in large domains, whereas the O-(2×2) structure exists for smaller coverages around 0.25 ML.

Recently, it has been proposed that under the cover of Gr, the adsorbate-metal interaction might be modified, thereby opening options to influence reactions or enable new ones in the confined space between the substrate and Gr [32-34]. Oxygen binds strongly to the Ir(111) substrate with an energy gain of more than 4 eV per oxygen adatom (referred to the energy of a free oxygen atom)[23-26] and, because it is saturated by its strong bond to Ir, binds only weakly to Gr [6, 18]. Therefore, one would at first glance not expect a noticeable effect of a Gr cover on the oxygen adsorbate phases bound to Ir(111). However, Larciprete *et al.* [7] found for the oxygen intercalation layer an unexpectedly high coverage above 0.6 ML and invoked as one possible explanation "the presence of graphene locking". Although we find no evidence for such a high saturation coverage, indeed we observe the Gr cover to influence the oxygen adsorbate ordering. Experimentally, we identify for the first time an O-($2\sqrt{3}\times2\sqrt{3}$)–R30° superstructure with a nominal coverage of θ = 0.5 ML. Moreover, we clarify the conditions of formation and provide a model for the previously reported O-($\sqrt{3}\times\sqrt{3}$)-R30° structure with θ = 0.33 ML [35]. Both adsorbate phases do not exist on bare Ir(111). The existence of these phases under graphene and their absence on bare Ir(111) demonstrates that the Gr cover plays a significant role in the stabilization of these superstructures. This effect of the graphene cover will be discussed in terms of possible changes in the oxygen chemisorption on Ir(111) due to the charge transfer existing from Gr to the oxygen intercalated layer.

Results

I. Oxygen adsorbed to bare Ir(111).

We firstly find it necessary to clear out the remaining uncertainty reported in Refs. [25, 31] and described above concerning the structure and saturation coverage of oxygen phases on bare Ir(111), *i.e.*, without Gr cover. Fig. 1 (a), (c), and (e) display scanning tunneling microscopy (STM) images acquired at room temperature after exposure of the Ir(111) surface to gas doses in the range of 400-750 L of molecular oxygen at 375 K, using a gas pressure of 1×10^{-5} mbar.

In the topograph in Fig. 1(a), obtained after exposure to 600 L O_2, a hexagonal array of protrusions with a periodicity of (0.54 ± 0.05) nm is observed. Since the lattice parameter of the Ir(111) surface is 0.27 nm, the symmetry and periodicity displayed in Fig. 1 (a) are consistent with an O-(2×2) superstructure. A ball model for the O-(2×2) superstructure with a saturation coverage θ = 0.25 ML, where the oxygen adatoms are placed in threefold coordinated sites, is displayed in Fig. 1 (b).

The STM image contrast of an O-adatom adsorbed to a metal surface is an intricate issue and needs to be addressed here. Depending on tip state and tunneling conditions an O-adatom is usually imaged as a dark depression, often of triangular shape, or occasionally also as a dark depression with a small bright protrusion in its center[36-45]. The (2×2) pattern of bright dots in Fig. 1(a) therefore is likely to result from the superposition leaving bright spots at locations where *no* adatoms are adsorbed [see also description of Fig. 2 (b)].

Fig. 1(c) presents an STM topograph acquired after exposure to 750 L O_2. Atomic rows are visible which are parallel to the dense-packed directions of Ir(111) and have a separation of (0.53 ± 0.05) nm. The separation is within the limits of error twice the spacing between dense-packed rows of Ir(111). The observed topography is therefore consistent with an O-(2×1) adsorbate structure. The corresponding ball model with a saturation coverage θ = 0.5 ML is shown in Fig. 1(d). Large scale images reveal a random distribution of the three equivalent rotational domains of the O-(2×1) superstructure over the entire Ir(111) surface.

However, in the STM topograph shown in Fig. 1(e) we observe a specific arrangement of the domains surrounding a strain defect. Atomic oxygen rows in the three different rotational domains are tangentially surrounding a bulge in the central part of the image. The bulge results from Xe implantation during sample cleaning followed by insufficient annealing, such that not all implanted gas had escaped to the vacuum [46]. In consequence, a subsurface gas bubble is created, deforming the surface near layers. Similar STM topographs have been previously reported by Gsell *et al.* after the adsorption of oxygen on Ru(0001) with subsurface noble gas bubbles [47]. According to these authors, the bubble-induced surface strain is responsible for the peculiar tangential orientation of the oxygen rows surrounding the deformation.

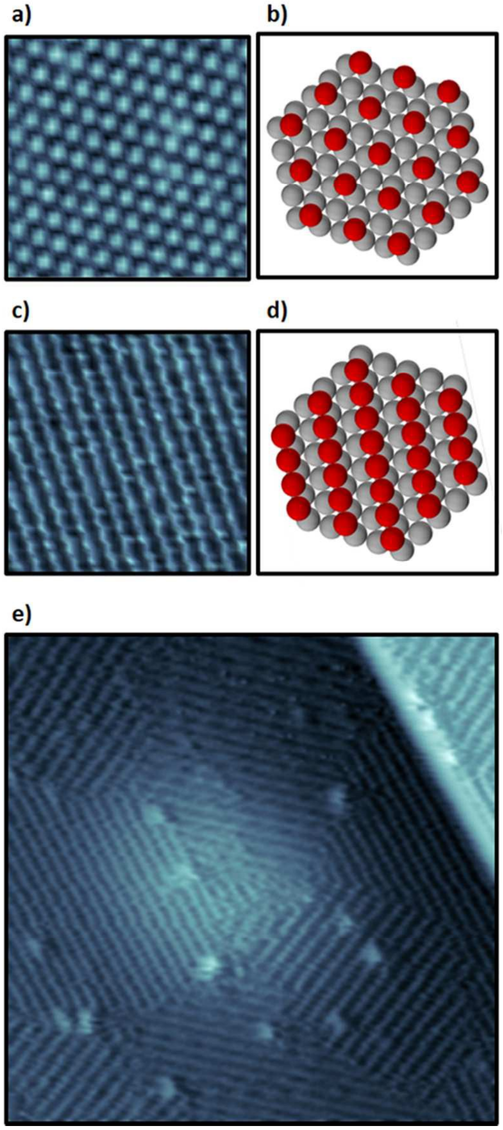

Fig. 1. (a) STM topograph of Ir(111) after exposure to 600 L molecular oxygen at 375 K. (b) Ball model proposed for the O-(2×2) superstructure observed in (a). Oxygen adatoms: red spheres; Ir atoms: gray spheres. (c) STM topograph after exposure to 750 L molecular oxygen at 375 K. (d) Ball model of the O-(2×1) structure in (c). (e) STM topograph after exposure to 400 L at 375 K. The central part displays a bulge due to a subsurface Xe bubble. See text. Tunneling parameters: (a) V_s = -1.5 V, I_T = 0.6 nA; size: 6×6 nm^2. (c) V_s = +0.98 V, I_T = 0.6 nA; size: 6×6 nm^2. (e) V_s = +0.98 V, I_T = 0.5 nA; size: 16×16 nm^2.

Consistent with the conclusions of Gsell *et al.*[47] for the case of oxygen adlayers chemisorbed on Ru(0001), our interpretation is as follows. Somewhat away from the bulge center, the atomic separation in the surface layer is reduced in radial direction (compression) and extended in tangential direction (elongation). Due to the repulsive dipole-dipole interaction of the negatively charged oxygen adsorbates along the (2x1) rows, the energy is minimized by arranging the rows tangentially around the bulge center.

Based on our STM topographs, there can hardly be any doubt that an O-(2×1) structure with a low concentration of defects and a coverage close to 0.5 ML is formed on Ir(111). We therefore attribute the low saturation coverage of $\theta = 0.38$ ML previously reported by Bianchi *et al.* to the fact that these authors adsorbed the oxygen at 80 K, where oxygen is immobile. Since an event of dissociative chemisorption requires two adjacent adsorption sites, in the absence of mobility the adsorbate layer must remain defective and saturation cannot be achieved. Here we used 375 K as oxygen adsorption temperature, where diffusion of oxygen adatoms is certainly present, since at this temperature oxygen adatoms already diffuse under Gr flakes on Ir(111) [6].

Finally, we note that atomic oxygen is readily reacted away from the sample surface through impinging CO or H_2 molecules. Therefore, the background pressure during and after oxygen exposure as well as the elapsed time since the O_2 exposure are more important for the structure observed than the exposure itself, given that saturation had been achieved.

II. Oxygen intercalation structures.

After having clarified the situation on bare Ir(111), we now investigate the case of oxygen intercalated under Gr on Ir(111). Our analysis of oxygen intercalation structures is based on the fact that STM is able to "see" the intercalation layer structures through the graphene cover. The apparent transparency of graphene has been already noticed a number of times and made it possible, for instance, to image the standing wave patterns of the Ir(111) [48, 49], Cu(111) [50] and Au(111) [50] surface states through Gr as well as to determine the structure of Eu and Cs intercalation layers under Gr on Ir(111) [11, 51].

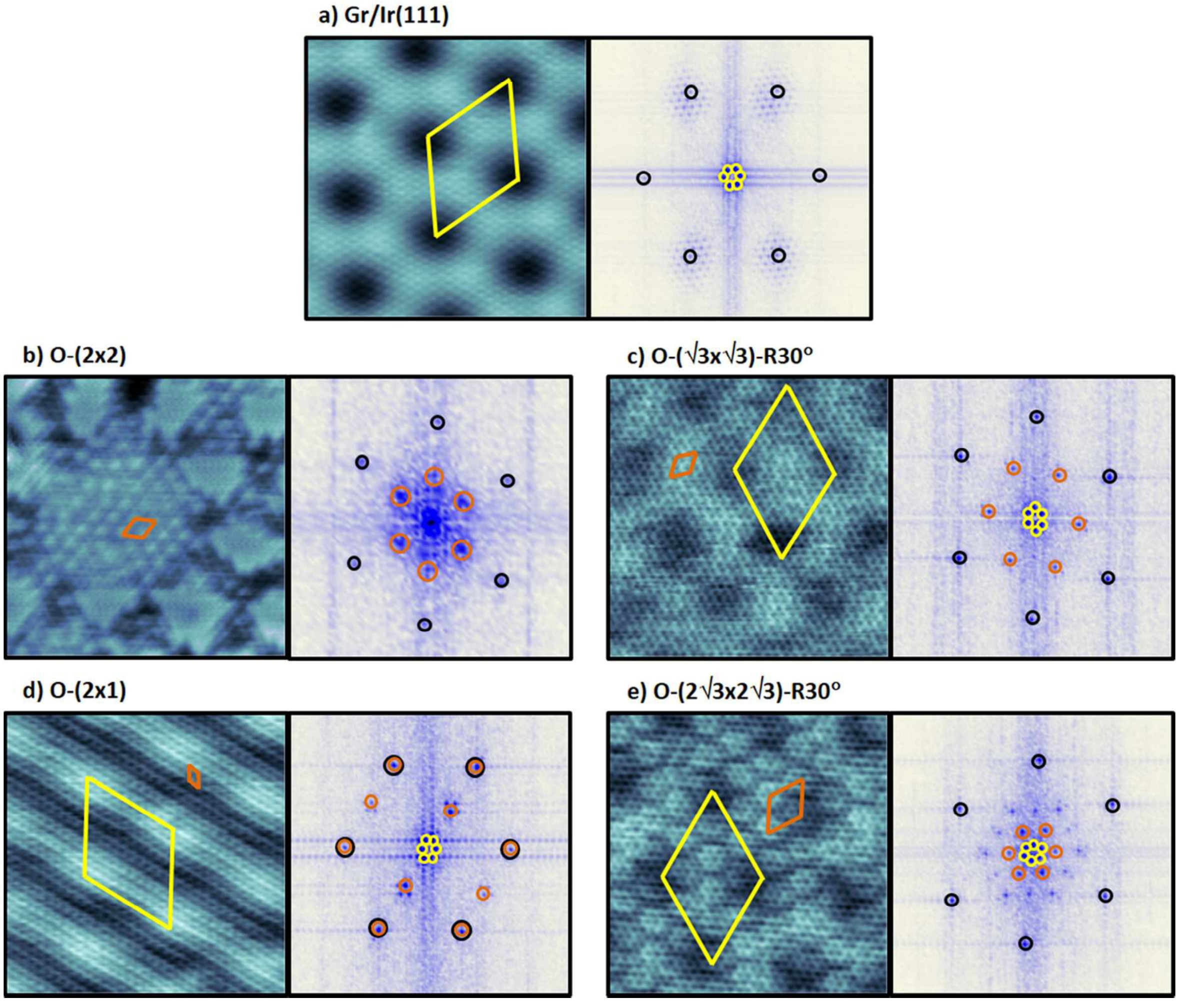

Fig. 2. STM topographs (left) and corresponding 2D-FFTs (right) of Gr/Ir(111) (a) without intercalated oxygen and (b)-(e) after oxygen intercalation for 600 s at 530 K. Oxygen pressures and exposures are: (b) 2.4×10^{-6} mbar and 1.1×10^3 L, (c),(d) 2.4×10^{-5} mbar and 1.1×10^4 L, as well as (e) 2.4×10^{-4} mbar and 1.1×10^5 L. In the topographs the moiré unit cell is indicated by a yellow, the oxygen superstructure unit cell by an orange diamond. In the 2D-FFTs the spots from the Gr lattice are encircled black, moiré spots yellow, and oxygen induced superstructure spots orange. Gr coverage is 0.8 ML, except for (c) where it amounts only to 0.5 ML. The image size is 7.5×7.5 nm^2 for all topographs. Tunneling parameters: (a) $V_s = +0.5$ V, $I_T = 0.1$ nA; (b) $V_s = +0.64$ V, $I_T = 0.8$ nA; (c) $V_s = -1.06$ V, $I_T = 0.02$ nA; (d) $V_s = +0.43$ V, $I_T = 0.1$ nA; (e) $V_s = +0.79$ V, $I_T = 0.3$ nA. Note that the images are slightly distorted by thermal drift, piezo creep, and differing scan directions.

Nanoscale RSCPublishing

ARTICLE

For reference, Fig. 2 (a) displays an atomically resolved STM topograph of the well-known Gr moiré with Ir(111). It forms an incommensurate superstructure of (10.32×10.32) Gr unit cells resting on (9.32×9.32) substrate Ir(111) unit cells [4]. The dense packed rows of Ir(111) and Gr are aligned with an orientational scatter below 0.5°. The apparent moiré corrugation in the STM topograph of Fig. 2 (a) is 0.14 nm**.** To the right of the topograph, its two-dimensional Fast Fourier transform (2D-FFT) is shown. The periodic lattices visible in the STM topograph give rise to sharp spots in the 2D-FFT representing their wave vectors. The spots corresponding to the periodicity of the moiré pattern are marked with yellow circles, and the spots corresponding to the Gr atomic lattice with black circles. In addition, satellite spots appear around the Gr spots, which are linear combinations of the wave vectors related to the atomic periodicity of Gr (within black circles) and the ones of the moiré superstructure (within yellow circles). They result from the nonlinear mixing of the two corrugations in the real space image, either *de facto* or due to the imaging process. Note also that depending on slight asymmetries of the imaging tip, the intensities of the equivalent spots in the 2D-FFT may depend on their orientation.

In order to intercalate oxygen under Gr/Ir(111), the Gr sheet must not be perfectly closed because some bare Ir surface is necessary to dissociatively adsorb O_2. The atomic oxygen then penetrates under Gr from the edges[6]. Therefore we prepared coalesced Gr films with holes and an approximate coverage of 0.8 ML for our experiments (see methods section). Because oxygen intercalation requires the delamination of Gr, an applied oxygen pressure during dosing at elevated temperatures is necessary. In Fig. 2, we show STM topographs from a series of experiments where we varied the oxygen exposure at constant exposure time from 1.1×10^3 L [in (b)] via 1.1×10^4 L [in (c) and (d)] to 1.1×10^5 L [in (e)]. The intercalation temperature was always 530 K.

At the lowest gas dose of 1.1×10^3 L [Fig. 2 (b)], patches of the O-(2×2) structure in the central part of the image coexist with bright, often triangular areas with moiré periodicity. It is thus obvious that the distribution of oxygen is not homogenous in this stage of intercalation. With O-adatoms appearing as dark features in the STM topograph [see discussion of Fig. 1(a)], the bright areas in the STM topograph are not intercalated by oxygen. Apparently, the inhomogeneous binding of Gr to Ir(111) is reflected in this intercalation pattern. A large scale topograph underlining this point is provided as Fig. S1 in the supporting information. For bare Ir(111), already at lower exposures a homogenous O-(2×2) superstructure may cover the entire sample with well ordered domains separated by translational boundaries. To the right of the STM topograph, we display its 2D-FFT with the Gr spots encircled in black and the O-(2×2) superstructure spots encircled in orange. Note that in the 2D-FFT the O-(2×2) spots do not sit at half-integer position with respect to the Gr spots, but about 10% more towards the origin. Using the atomic Gr spots for calibration, a superstructure periodicity of (0.54 ± 0.01) nm is found. Thus, the spots related to the O-atoms sit at half-integer position with respect to Ir(111), of which the lattice is invisible in the 2D-FFT.

Fig. 2 (c) displays an atomically resolved STM topograph after exposure of Gr/Ir(111) to 1.1×10^{-4} L of molecular oxygen. The oxygen-induced superstructure modulation in the Gr lattice is indicated by an orange diamond. The 2D-FFT displays 6 spots encircled in orange, which are due to an O-(√3×√3)–R30º superstructure. The superstructure periodicity is (0.45 ± 0.03) nm**,** consistent with the O-(√3×√3)–R30º structure, as observed by Craes *et al.* under Gr nanoflakes[35]. This structure has not been observed for oxygen adlayers on bare Ir(111). A structural model for the oxygen intercalation layer is proposed in the next section.

Fig. 2 (d) presents an entirely different structure of the O intercalation layer. The STM topograph displays lines running from the lower right to the upper left. They are parallel to the atomically resolved Gr rows, but possess approximately a spacing that is twice as large. In addition, the moiré periodicity is visible as bright protrusions. The moiré related corrugation normal to the line pattern is 0.04 nm, while parallel to it only 0.02 nm are measured. In the 2D-FFT to the right of the STM topograph, an O-(2×1) periodicity is resolved and indicated by orange circles. The unit cell dimensions based on the analysis of the 2D-FFT are 0.27 nm × 0.54 nm, as expected for a O-(2×1) superstructure with respect to Ir(111). The interpretation as a O-(2×1) superstructure is backed up by the fact that in other STM topographs (not shown) the line pattern is observed in 3 rotational domains with angles of 120° with respect to each other, as observed for the O-(2×1) superstructure on bare Ir(111) without the Gr cover in Fig. 1 (e). The O-(2×1) intercalation phase for Gr/O/Ir(111) has already been proposed on the basis of XPS and LEED measurements,[6, 31] but has not been observed directly.

We note that already for the exposure of 5×10^3 L the O-(2×1) is formed, but with very small domain sizes of the order of the moiré unit cell size (2.5 nm) and in coexistence with small patches of the O-(2×2) structure (see Fig. S2 in the supporting information).

Finally, upon increasing the oxygen exposure to 1.1×10^5 L an entirely new superstructure evolves. As shown in the atomically resolved STM topograph of Fig. 2 (e) the Gr lattice, the moiré and a flower type structure are visible. The latter we attribute to the oxygen intercalation layer. The entire corrugation resulting from the three periodicities is rather low, amounting only to 0.02 nm**.** The 2D–FFT right to the STM topograph displays, in addition to the Gr lattice and the moiré periodicity, an O-(2√3×2√3)–R30º structure with respect to Ir(111), encircled in orange. Based on the 2D-FFT we obtain a unit cell side length of 0.94nm ± 0.02 nm, in good agreement with our assignment. Due to the strong deviation of the O-(2√3×2√3)–R30º structure from a harmonic corrugation also spots corresponding to multiples of the fundamental reciprocal wavelength are visible. We note that the O-(2√3×2√3)–R30º and the O-(2×1) superstructure often coexist. The O-(2√3×2√3)–R30º structure is distinct from the O-(2×1) one by its higher symmetry, which results in the lack of rotational domains. Also, rather frequently, small patches of the O-(√3×√3)–R30º motif are found within extended areas of the O-(2√3×2√3)–R30º structure [compare to Fig. 2 (e), lower right]. The O-(2√3×2√3)–R30º structure has neither been reported before, nor been observed by us for oxygen adlayers on bare Ir(111). A structural model for the oxygen intercalation layer is proposed in the next section.

The absence of the O-(√3×√3)–R30º structure on bare Ir(111) can directly be visualized through images only partly covered by Gr. Fig.

3 (a) exhibits an atomically resolved STM topograph, where the lower right part is not covered by Gr. In this part two differently oriented domains of a defective O-(2×1) structure are visible. In the upper left part of the topograph Ir(111) is covered by Gr. There, the O-($\sqrt{3}\times\sqrt{3}$)–R30º structure is present, superimposed on a faint Gr moiré. The framed area in Fig. 3 (a) is magnified in Fig. 3 (b), where in addition to the O-($\sqrt{3}\times\sqrt{3}$)–R30º structure also the Gr lattice is resolved. The 2D-FFT in Fig. 3 (c) displays the spots characteristic for the Gr lattice and the O-($\sqrt{3}\times\sqrt{3}$)–R30º structure, as expected. Similar STM topographs display the coexistence of O-($2\sqrt{3}\times2\sqrt{3}$)–R30º structure under Gr and the O-(2×1) structure on bare Ir(111) (data not shown).

It is interesting to note that an oxygen intercalation layer of a lower coverage [O-($\sqrt{3}\times\sqrt{3}$)-R30º, θ = 0.33 ML] coexists with an oxygen ad-layer on the bare Ir(111) of higher coverage [O-(2×1), θ = 0.5 ML). Grånäs *et al.* [6] already noted that adsorption of atomic oxygen under Gr is energetically disfavored compared to adsorption on the bare Ir terrace: Oxygen is squeezed out from under the Gr as soon as there is space on the bare terrace. The same principle holds apparently in Fig. 3 (a).

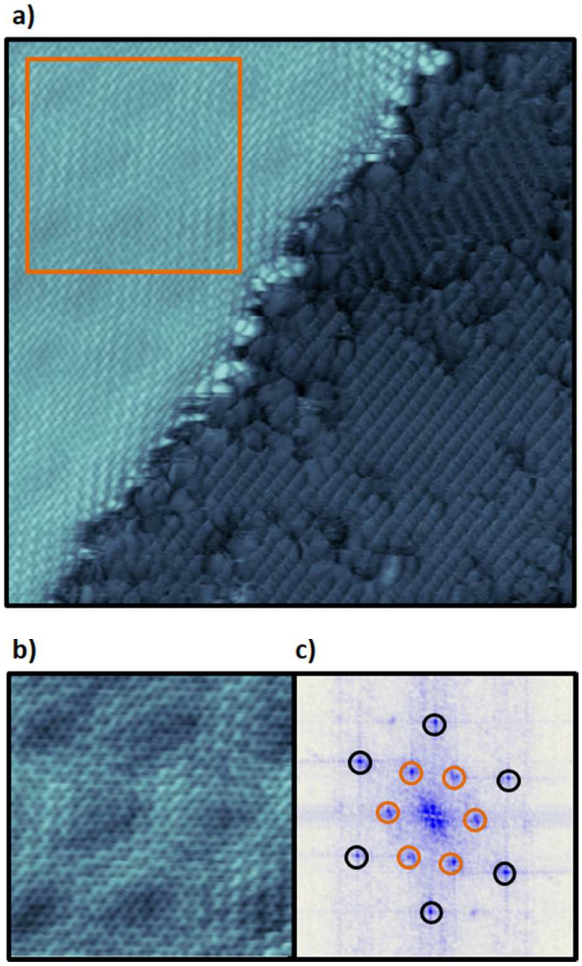

Fig. 3. (a) STM topograph of Ir(111) with 0.8 ML Gr after exposure to 1.4×10^4 L molecular oxygen at 530 K. Upper left: Gr covered with O-($\sqrt{3}\times\sqrt{3}$)–R30º intercalation structure. Lower right: bare Ir(111) with defective O-(2×1) structure. Tunneling parameters: V_s = -0.45 V, I_T = 0.02 nA; size: 18×18 nm^2. (b) Magnified view of the boxed area in (a). Size: 6.5×6.5 nm^2. (c) 2D-FFT of (b). Black and orange circles represent the periodicities of Gr and of the O-($\sqrt{3}\times\sqrt{3}$)–R30º superstructure, respectively.

III. Atomistic models for the O-($\sqrt{3}\times\sqrt{3}$)-R30º and O-($2\sqrt{3}\times2\sqrt{3}$)–R30º structures

In the following, tentative models for the oxygen ad-layer structures under Gr are proposed. For the O-($2\sqrt{3}\times2\sqrt{3}$)–R30º structure as shown in Fig. 2 (e), a supercell with 6 oxygen atoms (nominal coverage of θ = 0.5 ML) with the adatoms placed in equivalent threefold coordinated fcc hollow sites of the Ir(111) substrate is assumed. The ball model in Fig. 4 (a) visualizes our proposal. The resulting structure is considered as the superposition of two ad-layers with (2x2) [red spheres] and ($\sqrt{3}\times\sqrt{3}$)–R30º [blue spheres] symmetry, having one coinciding lattice point.

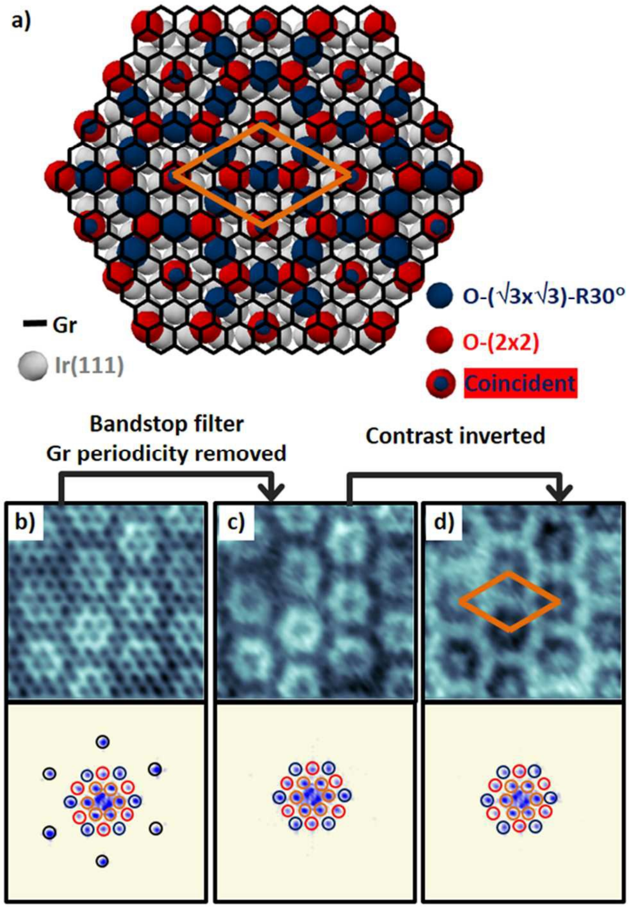

Fig. 4. (a) Ball model proposed for the O-($2\sqrt{3}\times2\sqrt{3}$)–R30º structure observed in Figs. 2 (e) and 4 (b) with six oxygen atoms per unit cell. The superstructure can be rationalized as the superposition of an O-($\sqrt{3}\times\sqrt{3}$)–R30º [blue spheres] and an O-(2×2) [red spheres] structure with one coinciding atom. (b) Atomically resolved STM topograph of the O-($2\sqrt{3}\times2\sqrt{3}$)–R30º structure. Tunneling parameters: V_s = 1.15 v, I_T = 0.3 nA; size = 3.1 × 3.1 nm^2. (c) Same as (b), but after removal of Gr periodicity through bandstop filtering in Fourier space. (d) Same as (c), but after contrast inversion. Under each topograph the corresponding 2D-FFT is shown. See text.

The assumption of oxygen adatom adsorption in threefold fcc hollow sites is based on previous work finding this adsorption site for atomic oxygen on bare Ir(111) [21, 23-26]. Coverage and placement of atoms is obtained from our STM topographs. The procedure employed to derive the proposed ball model is shown in the lower panel of Fig. 4. The atomically resolved STM topograph of Fig. 4 (b) with the O-($2\sqrt{3}\times2\sqrt{3}$)–R30º structure is bandstop filtered in reciprocal space to remove the Gr periodicity. The resulting topograph shown in Fig. 4 (c) is then contrast inverted and displayed in Fig. 4 (d), accounting for O adatoms being imaged as depressions by STM[36-45]. Thus, in the contrasted inverted image the bright protrusions are assumed to represent the locations of O adatoms. One could also place three O-adatoms instead of one into the center of the rings formed by the O-adatoms. This would bring the coverage to θ = 0.66 ML in line with the high coverage proposed by Larciprete *et al.*[7] for O intercalated Ir(111). However, this would require placing O-adatoms into threefold hollow sites of hcp character, inconsistent with what has been invariably been found for other O adlayers by DFT calculations[23-26]. Density functional theory calculations are therefore necessary to substantiate our proposed model for the O-(2√3×2√3)–R30º structure.

For the O-(√3×√3)–R30º structure as shown in Fig. 2 (c), a supercell with one oxygen adatom (nominal coverage of 0.33 ML) with the adatoms placed in equivalent threefold coordinated hollow sites of the Ir(111) substrate is suggested and visualized through the ball model in Fig. 5 (a). The same methodology as for the O-(2√3×2√3)–R30º structure is employed in Figs. 5 (b) - (d) to derive coverage and placement of oxygen adatoms.

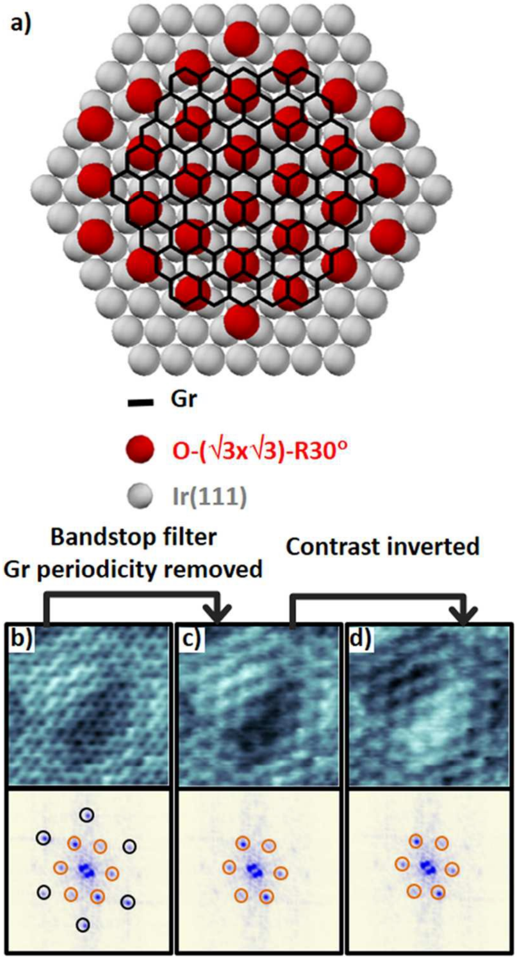

Fig. 5. (a) Tentative ball model for the O-(√3×√3)–R30 structure observed in Figs. 2 (c) and 5 (b) with one oxygen atom per unit cell. (b) Atomically resolved STM topograph of the O-(√3×√3)–R30 structure. Tunneling parameters: V_s = –0.45 V, I_T = 0.2 nA; size = 3.1 × 3.1 nm^2. (c) Topograph of (b) after removal of Gr periodicity through bandstop filtering in Fourier space. (d) Topograph of (c) after additional contrast inversion. Under each topograph the corresponding 2D-FFT is shown. See text.

IV. Temperature and pressure dependence of the intercalation layer

According to our model for the O-(2√3×2√3)–R30º structure outlined above, it has the same coverage θ = 0.5 ML as the O-(2×1) structure. The question arises by which circumstances the formation of one phase over the other is favored. We varied the exposure to molecular oxygen by an order of magnitude from 1.1×10^4 L to 1.1×10^5 L at fixed exposure time and the sample temperature during exposure by 40 K. Fig. 6 summarizes our observations.

At 490 K both phases coexist in domains with typical linear dimensions below 10 nm [see Figs. 6 (a) and (b)]. Based on a survey of all STM topographs of these experiments, there is a clear tendency for the formation of a larger fraction of the O-(2√3×2√3)–R30º for the higher oxygen exposure [Fig. 6 (b)]. As visible in Figs. 6 (a) and (b) it is invariably found that the areas of the O-(2√3×2√3)–R30º phase areas are bound by O-(2×1) domains of different orientation, i.e., there is never an O-(2√3×2√3)–R30º phase island embedded into a single large O-(2×1) domain. One might conclude that the O-(2√3×2√3)–R30º phase nucleates at the domain boundaries of O-(2×1) structure and expands the more, the higher the exposure.

Increasing the intercalation temperature to 530 K changes the picture. Now for the lower oxygen exposure the O-(2×1) phase is observed exclusively as intercalation structure [Fig. 6 (c)]. We also observe rotational domains of the O-(2×1) arranged tangentially around defects or gas bubbles in the substrate, similar to the situation on bare Ir (111) as shown in Fig. 1 (c). For the higher oxygen exposure the O-(2√3×2√3)–R30º structure dominates the images [Fig. 6 (d)]. Still small patches of O-(2×1) are observed, specifically close to step edges. This feature is likely to be related to uniaxial strain near steps. The domain size for both structures has increased substantially at 530 K, with a tendency for larger domains of the O-(2√3×2√3)–R30º. Also small patches of the O-(√3×√3)–R30º motif still can be identified, e.g. in Fig. 6 (d) in the lower right corner.

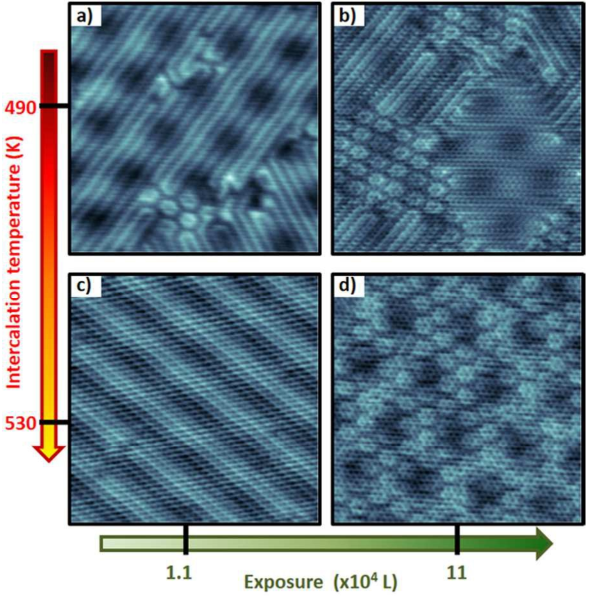

Fig. 6. (a)-(d) STM topographs of Gr/Ir(111) after oxygen intercalation at following pressures of molecular oxygen, exposures, and sample temperatures: (a) 2.4×10^{-5} mbar, 1.1×10^4 L, and 490 K; (b) 2.4×10^{-4} mbar; 1.1×10^5 L, and 490 K, (c) 2.4×10^{-5} mbar, 1.1×10^4 L, and 530 K; (d) 2.4×10^{-4} mbar, 1.1×10^5 L, and 530 K. Tunneling parameters: a) V_s = +1.15, I_T = 0.3 nA; b) V_s = +0.79 V, I_T = 0.3 nA; c) V_s = –1.12 V, I_T = 0.06 nA; d) V_s = +0.43 V, I_T = 0.1 nA. The image size is 7.5×7.5 nm^2 in all cases.

V. DFT calculations

In order to obtain insight, why the new O-(√3×√3)–R30º and O-(2√3×2√3)–R30º superstructures form under Gr, we conducted DFT calculations taking van der Waals interactions properly into account, as outlined in the Methods section. In all calculations O was adsorbed in the Ir(111) fcc hollow site, consistent with previous calculations [23-26]. The adsorption energies E_{ads} for the O-(2×2) and the O-(2×1) phase on bare Ir(111) specified in Table 1 agree quite well with the adsorption energies obtained in previous calculations by He *et al.*[52] and by Andersen *et al.*[53] for the same system. For the O-(√3×√3)–R30º structure, E_{ads} calculated by He *et al.* also matches to within 0.05 eV with our value of -1.83 eV. These data sets, as well as calculations where E_{ads} was referenced to atomic oxygen [24, 25], display a decrease in the strength of binding (increase of E_{ads}) with increasing coverage from 0.25 ML to 0.5 ML. This decrease may be attributed to a decrease in the number of Ir electrons per adsorbate O atom that are available for binding, and possibly in part also to an increasing repulsive electrostatic interaction of O atoms with a partial negative charge [52]. When plotting E_{ads} *per Ir(111) surface unit cell* (instead of per O atom) as a function of coverage the phase stability of the O-(√3×√3)–R30º phase can be analyzed on the basis of our DFT calculation. The thin dashed line connecting the data points in the plot displayed in Fig. 7 for the O-(2×2) and O-(2×1) superstructures represents the average adsorption energy per site for a system phase-separated into patches of the O-(2×2) and the O-(2×1) structures. The data point for the O-(√3×√3)–R30º structure is located above the thin dashed line, indicating that at a surface coverage of θ = 0.33 ML the phase-separated system has a lower E_{ads} (stronger binding) than a homogenous O-(√3×√3)–R30º phase, consistent with the experimental observation that only O-(2×2) and the O-(2×1) structures are observed experimentally.

We also relaxed the O-(2√3×2√3)–R30º superstructure and found it to be a stable energetic minimum, however energetically disfavored by 0.08 eV per oxygen atom compared to the O-(2×1) structure, which has nominally the same coverage. This result is consistent with the absence of the O-(2√3×2√3)–R30º structure on bare Ir(111).

Superstructure	E_{ads} (eV) O/Ir(111)	E_{ads} (eV) Gr/O/Ir(111)
2×2	-1.96	$-1.96 + 8\Delta E_C$
√3×√3-R30º	-1.83	$-1.85 + 6\Delta E_C$
2×1	-1.80	$-1.82 + 4\Delta E_C$
2√3×2√3-R30º	-1.72	$-1.74 + 4\Delta E_C$

Table 1: Adsorption energies calculated for oxygen adsorbed to Ir(111) and for oxygen intercalated between Gr and Ir(111). See text.

A similar set of calculations as for adsorption on bare Ir(111) was conducted for the intercalation structures. However, for technical reasons after removal of the oxygen atoms these calculations leave the Gr layer in its position, whereby E_{ads} is too low by an amount ΔE_C per C atom, which is gained when Gr moves to its new equilibrium position closer to the substrate. ΔE_C is of the order of a few 10 meV. Up to this correction, the adsorption energies of the intercalation structures are almost indistinguishable from the ones on the bare surface. E_{ads} *per Ir adsorption site* yields again, as for the bare surface, a marginal preference of the phase-separated system as compared to (√3×√3)–R30º structure. Note that the stability considerations are not affected by the correction ΔE_C, since it implies just a vertical shift in Fig. 7. The O-(2√3×2√3)–R30º superstructure is found to be a stable energetic minimum, but energetically disfavored by 0.08 eV per oxygen atom compared to the O-(2×1) intercalation structure.

Apparently, our 0 K DFT calculations are unable to grasp the decisive difference between adsorption on bare Ir(111) and the intercalation structures, that makes the (√3×√3)–R30º and the O-(2√3×2√3)–R30º structures stable around their temperature of formation. The reason for this may be rooted in the approximations of the calculations itself (see methods), the neglect of entropic effects as well as of the chemical potential applied, or even kinetic effects during phase formation. To turn it positively, our calculations indicate that the phase separated O-(2×2) and O-(2×1) system is at θ = 0.33 ML only marginally preferred compared to the (√3×√3)–R30º structure. Subtle differences in energy not reproduced in our calculations might therefore be decisive for structure selection (see Discussion). Moreover, the O-(2√3×2√3)–R30º structure was found to be a stable energetic minimum consistent with our structural model derived from the STM topographs.

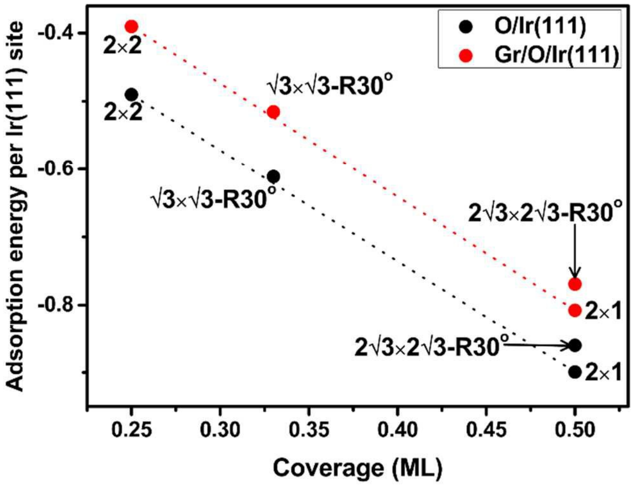

Fig. 7. Adsorption energies of oxygen per Ir lattice site on bare Ir(111) (black dots) and for intercalated oxygen (red dots) as a function of coverage. Thin dashed lines are the adsorption energies of a phase-separated system composed of O-(2×2) and the O-(2×1) structures in the coverage range from 0.25 ML to 0.5 ML. The data for Gr/O/Ir(111) are displaced by 0.1 eV towards more positive adsorption energies for better visibility. Therefore, the data points corresponding to Gr/O/Ir(111) represent the respective values of $E_{ads} - 2\Delta E_C + 0.1$ eV.

Discussion

We observe four different oxygen adsorbate phases under Gr, the O-(2×2) with θ = 0.25 ML, the O-(√3×√3)–R30º with θ = 0.33 ML, as well as the O-(2×1) and O-(2√3×2√3)–R30º structures both with θ = 0.5 ML. Prior to a discussion of what determines their occurrence we consider a number of experimental limitations in our studies.

First, the Gr coverage resulting from our recipe of preparation (compare Methods) has local and global variations in Gr coverage resulting in bare Ir(111) areas between 5% and 35%. On these areas dissociative adsorption of oxygen takes place and these areas will feed the intercalation of the Gr covered ones. It is therefore evident that (i) the oxygen exposure necessary to achieve saturation of adsorbed O under Gr is higher as for bare Ir(111) and (ii) variations in the uncovered area are relevant for the final structure that can be achieved. Second, oxygen adsorption at elevated temperatures (here around 500 K) is always counteracted by reactive oxygen removal through impinging CO or H_2 molecules from the background pressure. To this end it is important to work within the lowest possible background pressure and to minimize CO production at filaments during O exposure. Still after termination of exposure some oxygen might have been reacted away during cool down to temperatures were oxygen does not react anymore. This loss might affect the structures we observe. (iii) The structures under Gr presented here are "frozen" structures which are equilibrium structures in some temperature range, but it is uncertain whether these structures form at the intercalation temperature or only upon cooling.

Although STM is the ideal tool to uncover the richness of the adsorbate phase diagram under Gr and the high achievable perfection of the adlayers protected by Gr, it is evident from these remarks that *in situ* investigations using methods enabling structural determination while continuously tuning exposure, temperature and pressure of adsorption are necessary to obtain an accurate phase diagram.

Given this precaution, it seems that the oxygen exposure is the key parameter that decides on the sequence of structure with increasing coverage. The very large exposures needed to achieve these structures are attributed to the difficulty in filling the reservoir underneath Gr for kinetic and energetic reasons. Two kinetic factors are of relevance: First the size of feed areas providing atomic oxygen, and second the kinetic barrier for oxygen intercalation[6]. An energetic factor of relevance is the reduced binding energy of oxygen under Gr. Consistent with our calculations, it has been pointed out by Grånäs *et al.*[6] that O is squeezed out from under Gr as soon as O is removed from the adjacent bare Ir(111) areas.

Since we varied the oxygen exposure at fixed exposure time, simultaneously with the exposure also the applied oxygen pressure varied, which itself defines the gas phase chemical potential. Since we were not conducting *in situ* equilibrium experiments, we are not able to decide whether an adsorption-desorption equilibrium is established close to saturation around 0.5 ML and thus whether the gas phase chemical potential is of relevance or only the exposure. Specifically for the two phases of nominally identical coverage close to saturation, the O-(2×1) and O-(2√3×2√3)–R30º structures with $\theta = 0.5$ ML, it is quite plausible that indeed the applied pressure could be relevant for phase formation.

Both the O-(√3×√3)–R30º and the O-(2√3×2√3)–R30º phase have not been observed and are likely not to exist on bare Ir(111), in agreement with our DFT calculations. Since our DFT calculations do not predict their existence under Gr, we can only speculate why they are actually formed under Gr. As a starting point of our considerations we note that when the coverages exceeds 0.25 ML, patches of the O-(2×1) must be formed on bare Ir(111). This coexistence of O-(2×2) and O-(2×1) under Gr have been experimentally observed in STM images as those shown in Fig. S2. One relevant fact in this respect is the repulsive dipole-dipole interaction of the negatively charged oxygen adatoms that tends to diminish the adsorption energy within the O-(2×1) layer [20, 23, 25]. Still, the most favorable way for the system to deal with the repulsive dipole-dipole interaction of the O-adatoms is the formation of dense packed rows. However, with row formation a symmetry reduction compared to the substrate takes place and uniaxial strain domains are induced into the substrate. The total strain energy will grow with the average domain size. The interaction of the O-(2×1) with the strain fields of gas bubbles [compare to Fig. 1 c)] and steps proves the relevance of this energy penalty for structure formation in the O-(2×1). Evidently, this strain energy penalty is reduced by the formation of the more isotropic O-(√3×√3)–R30º and O-(2√3×2√3)–R30º structures with the same symmetry as the substrate. Note also that the strain energy limitation requires the presence of domain boundaries for the O-(2×1), while this is not the case for the O-(2√3×2√3)–R30º structure. Apparently, the presence of Gr reduces some other energetic disadvantages associated to these structures that prevent their formation on bare Ir(111). A modification of the repulsive dipole-dipole interaction of the O adsorbates through Gr and charge transfer between Gr and the O adsorbates [7, 18] must be considered as relevant factor in this respect.

Finally we come back to the question how the phases of nominally identical coverage (according to our model) are selected. On the basis of our STM measurements, the O-(2√3×2√3)–R30º structure is preferred over the O-(2×1) structure through higher exposure (or larger applied pressure). Therefore, it seems most probable that the former allows the system to approach the nominal coverage somewhat closer. While the O-(2×1) requires a certain number of rotational domain boundaries to limit uniaxial strain energy, this is not the case for the O-(2√3×2√3)–R30º. Therefore larger domains, i. e., a structure with less defects and thus a slightly larger adsorbed amount could be achieved for the O-(2√3×2√3)–R30º structure.

Assuming a larger nominal coverage for the (2√3×2√3)–R30º structure (e.g. of 0.67 ML in contradiction to our model) would certainly also explain the selection of this structure for enhanced exposure. However, we consider this assumption as implausible, as we observe the O-(2√3×2√3)–R30º structure to coexist with the O-(2×1) phase under Gr while at the same time on bare Ir(111) only the O-(2×1) structure can be observed.

O-(2×2) and O-(2×1) superstructures have also been reported for chemisorbed oxygen adlayers on other dense packed transition metal surface like Ru(0001) [54-58], Rh(111) [43] and Pt(111) [59-61]. These structures were also observed for intercalated oxygen on Gr/Ru(0001) [62]. Based on the generality of our considerations we propose that also for these substrates other, hitherto unobserved oxygen intercalation phases exist, possibly even the same new superstructures we described here.

Methods

The experiments were performed in an ultrahigh vacuum (UHV) system equipped with a home-built scanning tunneling microscope (STM) suitable for imaging in the temperature range from 20 K - 700 K [63, 64]. For gas exposure (molecular oxygen and ethylene) a dosing tube was used, with 10 mm diameter and ending about 5 cm in front of the sample. Therefore, the local pressure at the sample is enhanced by a factor $f = 80$ compared to the reading of the ion gauge[65]. In the following, we always specify the pressure at the sample, i.e. the ion gauge reading multiplied by the enhancement factor f. Ir(111) was prepared by sputtering at room temperature with 5 keV Xe^+ ions under 75° with respect to the surface normal, glowing in an oxygen partial pressure of 8×10^{-6} mbar at 1170 K, and subsequent flash annealing to 1520 K. For Gr growth, ethylene adsorbed at room temperature was dehydrogenated by flash annealing at 1520 K[65]. Subsequently, the resulting Gr islands were grown to an almost closed layer by exposing the sample at 1170 K for 180 s to a partial pressure of 8×10^{-7} mbar ethylene. A Gr coverage of about (80±15) % results. This methodology has previously been shown to lead to the exclusive growth of aligned Gr, i.e., with the dense-packed rows of Gr parallel to the ones of the substrate[5]. Additional direct evidence that our measurements were performed only over aligned Gr can be found in the fact that all of our STM images acquired on the Gr/O/Ir(111) interface display a unique moiré pattern (Note the alignment of the moiré spots and the Gr spots in the 2D-FFT's of the topographs in Figure 2.) For intercalation a fixed O_2 exposure time of 600 s was used. After the exposure pressure had been adjusted, the ion gauge was turned off to prevent excessive CO production at the hot filament. The exposure ranging from 1.4×10^3 L to 1.4×10^5 L was adjusted through a variation of the oxygen partial pressure from 2.4×10^{-6} mbar to 2.4×10^{-4} mbar. Exposure temperatures of 490 K and 530 K were used, which enable safe intercalation without etching of coalesced Gr films or large Gr flakes. Finally, STM imaging was performed with the sample at 300 K (Fig. 1) or 120 K (Figs. 2-6), and the images have been processed using the WSxM software [66]. Sample bias V_s and tunneling current I_T are specified for each topograph.

The O-adsorbed Ir(111) and O-intercalated Gr/Ir(111) systems have been investigated in the framework of DFT [67] by employing the projector augmented wave method[68] used to generate pseudopotentials with the Perdew-Burke-Ernzerhof exchange correlation functional[69]. To properly account for the van der Waals (vdW) interactions present in these systems, the corresponding ground-state geometries and adsorption energies have been obtained by considering a non-local correlation energy functional[70,71] as implemented by Klimeš *et al.*[72] in the VASP code[73,74] together with a recently developed exchange functional[75]. The Gr/O/Ir(111) geometry was modeled by a slab consisting of 5 atomic layers of unstrained Ir, oxygen adsorbed to Ir and a Gr layer atop, which was strained to match the Ir(111) surface lattice. Furthermore, for an energy cut-off energy of 450 eV and a Brillouin zone sampling by a mesh of 11×11×1 (√3×√3 geometry) and 6×6×1 (2×2 geometry), the non-intercalated and O-intercalated relaxed geometries were obtained when the calculated forces acting on the Gr, O and the two Ir topmost layers were less than 1 meV/Å.

The adsorption energy for oxygen chemisorbed to bare Ir(111) is

$$E_{ads} = [E_{OIr} - (E_{Ir} + n/2 \cdot E_{O2})]/n \qquad (1)$$

where E_{OIr} is the energy of the full system, E_{Ir} the energy of the Ir slab, n the total number of oxygen atoms employed in the calculation and E_{O2} the total energy of a free oxygen molecule in the gas phase.

Likewise, the adsorption energy for intercalated oxygen is

$$E_{ads} = [E_{GrOIr} - (E_{GrIr} + n/2 \cdot E_{O2})]/n + m\Delta E_C \qquad (2)$$

Here, E_{GrOIr} represents the energy of the full system including the Ir substrate, the oxygen intercalation layer and the Gr cover. E_{GrIr} is the energy of the Gr layer and the Ir slab underneath after removal of the intercalated oxygen keeping the Gr sheet in that height above Ir which it had when oxygen was intercalated. Naturally, this height is artificial, and the system will gain energy when Gr moves down to its new equilibrium distance above Ir. This energy is $m\Delta E_C$, where m is the number of C atoms related to one intercalated oxygen atom and ΔE_C the energy gain per C atom.

Conclusions

Based on atomic resolution STM imaging and Fourier analysis of oxygen intercalation layers under Gr we propose structural models for the O-(√3×√3)–R30° and O-(2√3×2√3)–R30° phases that do not exist on Ir(111) without a Gr cover for the range of experimental parameters investigated by us.

For Gr layers on Ir(111) we find with increasing oxygen exposure non-intercalated Gr, O-(2×2), O-(√3×√3)–R30°, O-(2×1), and O-(2√3×2√3)–R30° structures. Neighboring phases in coverage as well as phases of nominally identical coverage were found to coexist with each other. We speculated that the changes of the repulsive oxygen-oxygen interaction under the Gr cover might give rise to subtle energy changes that disfavor the O-(2×1) structure compared to the O-(2√3×2√3)–R30° for enhanced temperature and very close to the nominal saturation coverage of 0.5 ML.

The DFT calculations correctly predict the absence of the O-(√3×√3)–R30° and O-(2√3×2√3)–R30° superstructures for bare Ir(111), but surprisingly do not show an energetic preference of these structures under Gr. Apparently more sophisticated theoretical modeling is necessary.

The authors are convinced that the methodology presented here – imaging intercalation structures through the Gr cover combined with Fourier analysis – as well as the key finding - the existence of new adsorbate phases under the Gr cover – are relevant also for other Gr/metal systems.

Acknowledgements

Financial support through the European Commission by a Marie Curie Fellowship (Proposal 332214 ELECTROMAGRAPHENE), through the Institutional Strategy of the University of Cologne within the German Excellence Initiative and through the DFG Priority Program 1459 "Graphene" within Project No. MI581/20-1 is gratefully acknowledged. N. A. and V. C. gratefully acknowledge financial support from the Volkswagen-Stiftung through the "Optically Controlled Spin Logic" project.

Notes and references

[a] II. Physikalisches Institut, Universität zu Köln, Germany.

[b] Peter Grünberg Institute and Institute for Advanced Simulation, Forschungszentrum Jülich, Germany.

1. J. Wintterlin and M. L. Bocquet, *Surf. Sci.*, 2009, **603**, 1841-1852.
2. M. Batzill, *Surf. Sci. Rep.*, 2012, **67**, 83-115.
3. J. Coraux, A. T. N'Diaye, C. Busse and T. Michely, *Nano Lett.*, 2008, **8**, 565-570.
4. A. T. N'Diaye, J. Coraux, T. N. Plasa, C. Busse and T. Michely, *New J. Phys.*, 2008, **10**, 043033.
5. R. van Gastel, A. T. N'Diaye, D. Wall, J. Coraux, C. Busse, N. M. Buckanie, F. -J. Meyer zu Heringdorf, M. Horn- von Hoegen, T. Michely and B. Poelsema, *Appl. Phys. Lett.*, 2009, **95**, 121901.
6. E. Grånäs, J. Knudsen, U. A. Schröder, T. Gerber, C. Busse, M. A. Arman, K. Schulte, J. N. Andersen and T. Michely, *ACS Nano*, 2012, **6**, 9951-9963.
7. R. Larciprete, S. Ulstrup, P. Lacovig, M. Dalmiglio, M. Bianchi, F. Mazzola, L. Hornekær, F. Orlando, A. Baraldi, P. Hofmann and S. Lizzit, *ACS Nano*, 2012, **6**, 9551-9558.
8. L. Meng, R. T. Wu, H. T. Zhou, G. Li, Y. Zhang, L. F. Li, Y. L. Wang and H. J. Gao, *Appl. Phys. Lett.*, 2012, **100**, 083101.
9. E. Grånäs, M. Andersen, M. A. Arman, T. Gerber, B. Hammer, J. Schnadt, J. N. Andersen, T. Michely and J. Knudsen, *J. Phys. Chem. C*, 2013, **117**, 16438-16447.
10. S. Schumacher, T. O. Wehling, P. Lazić, S. Runte, D. F. Förster, C. Busse, M. Petrović, M. Kralj, S. Blügel, N. Atodiresei, V. Caciuc and T. Michely, *Nano Lett.*, 2013, **13**, 5013-5019.
11. S. Schumacher, D. F. Förster, M. Rösner, T. O. Wehling and T. Michely, *Phys. Rev. Lett.*, 2013, **110**, 086111.
12. R. Decker, J. Brede, N. Atodiresei, V. Caciuc, S. Blügel and R. Wiesendanger, *Phys. Rev. B*, 2013, **87**, 041403.
13. L. F. Li, Y. L. Wang, L. Meng, R. T. Wu and H. J. Gao, *Appl. Phys. Lett.*, 2013, **102**, 093106.
14. D. Pacile, P. Leicht, M. Papagno, P. M. Sheverdyaeva, P. Moras, C. Carbone, K. Krausert, L. Zielke, M. Fonin, Y. S. Dedkov, F. Mittendorfer, J. Doppler, A. Garhofer and J. Redinger, *Phys. Rev. B*, 2013, **87**, 035420.
15. L. Huang, W.-Y. Xu, Y.-D. Que, J.-H. Mao, L. Meng, L.-D. Pan, G. Li, Y.-L. Wang, S.-X. Du, Y.-Q. Liu and H.-J. Gao, *Chinese Physics B*, 2013, **22**, 096803.

16. E. Starodub, N. C. Bartelt and K. F. McCarty, *J. Phys. Chem. C*, 2010, **114**, 5134-5140.
17. C. Gómez-Navarro, R. T. Weitz, A. M. Bittner, M. Scolari, A. Mews, M. Burghard and K. Kern, *Nano Lett.*, 2007, **7**, 3499-3503.
18. W. Jolie, F. Craes, M. Petrovic, N. Atodiresei, V. Caciuc, S. Blügel, M. Kralj, T. Michely and C. Busse, *Phys. Rev. B*, 2014, **89**, 155435.
19. J. T. Grant, *Surf. Sci.*, 1971, **25**, 451-456.
20. V. P. Ivanov, G. K. Boreskov and V. I. Savchenko, W. F. Egelhoff Jr. and W. H. Weinberg, *Surf. Sci.*, 1976, **61**, 207-220.
21. C. M. Chan and W. H. Weinberg, *J. Chem. Phys.*, 1979, **71**, 2788-2792.
22. W.-H. Chung, D.-S. Tsai, L.-J. Fan, Y.-W. Yang and Y.-S. Huang, *Surf. Sci.*, 2012, **606**, 1965-1971.
23. Y. Xu and M. Mavrikakis, *J. Chem. Phys.*, 2002, **116**, 10846-10853.
24. W. P. Krekelberg, J. Greeley and M. Mavrikakis, *J. Phys. Chem. B*, 2004, **108**, 987-994.
25. H. Zhang, A. Soon, B. Delley and C. Stampfl, *Phys. Rev. B*, 2008, **78**, 045436.
26. S. D. Miller, N. Inoglu and J. R. Kitchin, *J. Chem. Phys.*, 2011, **134**, 104709.
27. P. A. Zhdan, G. K. Boreskov, A. I. Boronin, W. F. Egelhoff Jr. and W. H. Weinberg, *Surf. Sci.*, 1976, **61**, 25-36.
28. D. I. Hagen, B. E. Nieuwenhuys, G. Rovida and G. A. Somorjai, *Surf. Sci.*, 1976, **57**, 632-650.
29. T. S. Marinova and K. L. Kostov, *Surf. Sci.*, 1987, **185**, 203-212.
30. J. E. Davis, P. D. Nolan, S. G. Karseboom and C. B. Mullins, *J. Chem. Phys.*, 1997, **107**, 943-952.
31. M. Bianchi, D. Cassese, A. Cavallin, R. Comin, F. Orlando, L. Postregna, E. Golfetto, S. Lizzit and A. Baraldi, *New J. Phys.*, 2009, **11**, 063002.
32. P. Sutter, J. T. Sadowski and E. A. Sutter, *J. Am. Chem. Soc.*, 2010, **132**, 8175-8179.
33. R. Mu, Q. Fu, L. Jin, L. Yu, G. Fang, D. Tan and X. Bao, *Angew. Chem.-Int. Ed.*, 2012, **51**, 4856-4859.
34. Y. Yao, Q. Fu, Y. Y. Zhang, X. Weng, H. Li, M. Chen, L. Jin, A. Dong, R. Mu, P. Jiang, L. Liu, H. Bluhm, Z. Liu, S. B. Zhang and X. Bao, *Proc. Natl. Acad. Sci. U. S. A.*, 2014, **111**, 17023-17028.
35. F. Craes, S. Runte, J. Klinkhammer, M. Kralj, T. Michely and C. Busse, *Phys. Rev. Lett.*, 2013, **111**, 056804.
36. N. D. Lang, *Phys. Rev. Lett.*, 1986, **56**, 1164-1167.
37. H. Brune, J. Wintterlin, J. Trost, G. Ertl, J. Wiechers and R. J. Behm, *J. Chem. Phys.*, 1993, **99**, 2128-2148.
38. S. Esch, M. Hohage, T. Michely and G. Comsa, *Phys. Rev. Lett.*, 1994, **72**, 518-521.
39. P. Sautet, *Surf. Sci.*, 1997, **374**, 406-417.
40. T. Zambelli, J. V. Barth, J. Wintterlin and G. Ertl, *Nature*, 1997, **390**, 495-497.
41. B. C. Stipe, M. A. Rezaei, W. Ho, S. Gao, M. Persson and B. I. Lundqvist, *Phys. Rev. Lett.*, 1997, **78**, 4410-4413.
42. J. Trost, H. Brune, J. Wintterlin, R. J. Behm and G. Ertl, *J. Chem. Phys.*, 1998, **108**, 1740-1747.
43. S. Marchini, C. Sachs and J. Wintterlin, *Surf. Sci.*, 2005, **592**, 58-64.
44. J. M. Blanco, C. González, P. Jelinek, J. Ortega, F. Flores, R. Pérez, M. Rose, M. Salmeron, J. Méndez, J. Wintterlin and G. Ertl, *Phys. Rev. B*, 2005, **71**, 113402.
45. S. P. Devarajan, J. A. J. Hinojosa and J. F. Weaver, *Surf. Sci.*, 2008, **602**, 3116-3124.
46. T. Michely and G. Comsa, *Nucl. Instrum. Methods Phys. Res. Sect. B-Beam Interact. Mater. Atoms*, 1993, **82**, 207-219.
47. M. Gsell, P. Jakob and D. Menzel, *Science*, 1998, **280**, 717-720.
48. D. Subramaniam, F. Libisch, Y. Li, C. Pauly, V. Geringer, R. Reiter, T. Mashoff, M. Liebmann, J. Burgdörfer, C. Busse, T. Michely, R. Mazzarello, M. Pratzer and M. Morgenstern, *Phys. Rev. Lett.*, 2012, **108**, 046801.
49. S. J. Altenburg, J. Kröger, T. O. Wehling, B. Sachs, A. I. Lichtenstein and R. Berndt, *Phys. Rev. Lett.*, 2012, **108**, 206805.
50. A. J. Martínez-Galera, I. Brihuega and J. M. Gómez-Rodríguez, *Nano Lett.*, 2011, **11**, 3576-3580.
51. M. Petrović, I. S. Rakić, S. Runte, C. Busse, J. T. Sadowski, P. Lazić, I. Pletikosić, Z. -H. Pan, M. Milun, P. Pervan, N. Atodiresei, R. Brako, D. Šokčević, T. Valla, T. Michely and M. Kralj, *Nat. Commun.*, 2013, **4**, 2772.
52. Y. B. He, A. Stierle, W. X. Li, A. Farkas, N. Kasper and H. Over, *J. Phys. Chem. C*, 2008, **112**, 11946-11953.
53. M. Andersen, L. Hornekær and B. Hammer, *Phys. Rev. B*, 2014, **90**, 155428.
54. P. Piercy and H. Pfnür, *Phys. Rev. Lett.*, 1987, **59**, 1124-1127.
55. M. Lindroos, H. Pfnür, G. Held and D. Menzel, *Surf. Sci.*, 1989, **222**, 451-463.
56. H. Pfnür, G. Held, M. Lindroos and D. Menzel, *Surf. Sci.*, 1989, **220**, 43-58.
57. C. Stampfl and M. Scheffler, *Phys. Rev. B*, 1996, **54**, 2868-2872.
58. K. Meinel, H. Wolter, C. Ammer, A. Beckmann and H. Neddermeyer, *J. Phys.-Condes. Matter*, 1997, **9**, 4611-4619.
59. H. P. Bonzel and R. Ku, *Surf. Sci.*, 1973, **40**, 85-101.
60. N. Materer, U. Starke, A. Barbieri, R. Döll, K. Heinz, M. A. Van Hove and G. A. Somorjai, *Surf. Sci.*, 1995, **325**, 207-222.
61. H. Tang, A. Van der Ven and B. L. Trout, *Phys. Rev. B*, 2004, **70**, 045420.
62. K. Katsiev, Y. Losovyj, Z. Zhou, E. Vescovo, L. Liu, P. A. Dowben and D. W. Goodman, *Phys. Rev. B*, 2012, **85**, 195405.
63. M. Bott, T. Michely and G. Comsa, *Rev. Sci. Instrum.*, 1995, **66**, 4135-4139.
64. T. Michely, M. Kaiser and M. J. Rost, *Rev. Sci. Instrum.*, 2000, **71**, 4461-4467.
65. J. Coraux, A. T. N'Diaye, M. Engler, C. Busse, D. Wall, N. Buckanie, F. -J. Meyer zu Heringdorf, R. van Gastel, B. Poelsema and T. Michely, *New J. Phys.*, 2009, **11**, 023006.
66. I. Horcas, R. Fernández, J. M. Gómez-Rodríguez, J. Colchero, J. Gómez-Herrero and A. M. Baro, *Rev. Sci. Instrum.*, 2007, **78**, 013705.
67. P. Hohenberg and W. Kohn, *Phys. Rev.*, 1964, **136**, B864-B871.
68. P. E. Blöchl, *Phys. Rev. B*, 1994, **50**, 17953-17979.
69. J. P. Perdew, K. Burke, and M. Ernzerhof, *Phys. Rev. Lett.*, 1996, **77**, 3865-3868.
70. M. Dion, H. Rydberg, E. Schröder, D. C. Langreth and B. I. Lundqvist, *Phys. Rev. Lett.*, 2004, **92**, 246401.
71. K. Lee, É. D. Murray, L. Kong, B. I. Lundqvist and D. C. Langreth, *Phys. Rev. B*, 2010, **82**, 081101(R).

72. J. Klimeš, D.R. Bowler, and A. Michaelides, *Phys. Rev. B*, 2011, **83**, 195131.
73. G. Kresse and J. Hafner, *Phys. Rev. B*, 1994, **49**, 14251-14269.
74. G. Kresse and J. Furthmüller, *Phys. Rev. B*, 1996, **54**, 11169-11186.
75. I. Hamada, *Phys. Rev. B*, 2014, **89**, 121103(R).

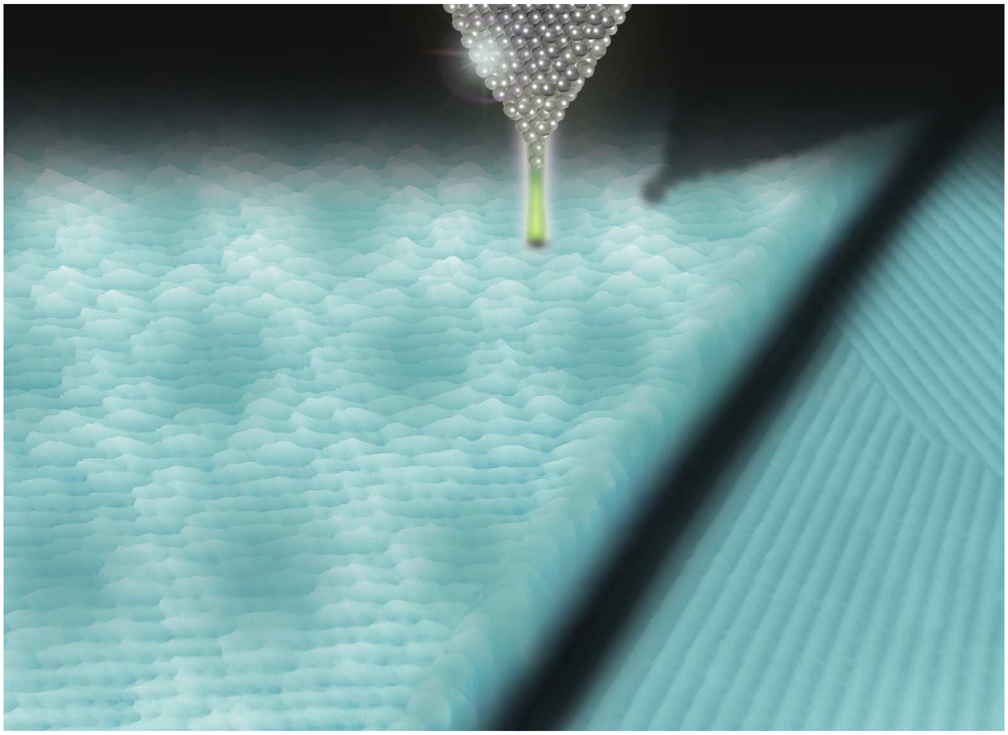

Artistic illustration of the results of the research performed by the II. Physikalisches Institut of the Universität zu Köln and, the Peter Grünberg Institute and Institute for Advanced Simulation of the Forschungszentrum Jülich, Germany.

The graphene cover induces a new atomic arrangement of oxygen chemisorbed on Ir(111).

Comparative study of the structural properties of oxygen monolayers chemisorbed on Ir(111) with and without the graphene cover. The existence of a new adsorbate phase for oxygen on Ir(111) when a Gr layer is on top is demonstrated.

186x135mm (300 x 300 DPI)